Approaching the Intrinsic Electron Mobility Limit of Bilayer MoS_2 via a Combined Twist-Angle and Stress-Engineering Strategy

Chennan Song(宋晨楠)[1] and Yu Xie(谢禹)[1,2*]

[1]*Key Laboratory of Material Simulation Methods & Software of Ministry of Education, College of Physics, Jilin University, Changchun 130012, China*
[2]*Key Laboratory of Physics and Technology for Advanced Batteries, Ministry of Education, College of Physics, Jilin University, Changchun 130012, China*

(Received 13 December 2025; accepted manuscript online 14 February 2026)

Bilayer MoS_2 is a promising channel candidate for extending Moore's law, owing to its optimal channel thickness and improved suppression of extrinsic scattering compared to monolayers. However, its intrinsic phonon-limited electron mobility is severely limited by enhanced K–Q intervalley scattering arising from the multivalley conduction band feature inherent to the bilayer structure. To overcome this bottleneck, we propose a "valley separation engineering" strategy that combines a twist angle near 30° with applied stress. Our first-principles calculations demonstrate that although valley separation can be continuously increased using this strategy, the electron mobility saturates at $\sim$200 $cm^2 \cdot V^{-1} \cdot s^{-1}$. The saturation is attributed to the competition between the reduced effective mass and enhanced intravalley scattering induced by phonon softening once the detrimental intervalley scattering is effectively suppressed by sufficient valley separation. This study establishes a theoretical upper limit for the intrinsic electron transport of bilayer MoS_2 masked by severe intervalley scattering.

DOI: 10.1088/0256-307X/43/3/030718 CSTR: 32039.14.0256-307X.43.3.030718

The continuous scaling of field-effect transistors (FETs) to meet the demands for higher performance, as described by Moore's law,[1] requires shrinking the channel length. However, aggressive scaling leads to detrimental short-channel effects (SCEs), such as high leakage currents. A fundamental strategy to mitigate these SCEs requires further reduction in the channel thickness.[2] For conventional three-dimensional (3D) bulk semiconductors, this strategy faces critical challenges: the process of decreasing the thickness (or fin width) inevitably introduces finite thickness variations, surface roughness, and dangling bonds. Such non-ideal factors cause severe carrier scattering and lead to a significant decrease in carrier mobility.[3,4] Two-dimensional (2D) semiconductors are among the potential candidates for this continuous scaling.[5] Owing to their natural layered structure in which the layers are connected by van der Waals forces without surface dangling bonds, 2D materials can be reduced to a thickness of a few atoms while maintaining their carrier mobility without a significant decrease.[4,6] These unique properties make 2D materials promising platforms for advanced device research.[7,8]

Layered MoS_2, as a representative 2D transition metal dichalcogenides (TMDs), has attracted widespread research interest because of its suitable bandgap and the successful synthesis of large-area films.[9–11] Although theoretical predictions for the room-temperature intrinsic phonon-limited electron mobility are in the range of 130–410 $cm^2 \cdot V^{-1} \cdot s^{-1}$,[12,13] early experimental values for monolayer (ml) MoS_2 were limited to $\sim$10 $cm^2 \cdot V^{-1} \cdot s^{-1}$. This discrepancy is largely attributed to dominant extrinsic scattering from sources such as Coulomb impurities, atomic defects, and polar surface optical phonons in the dielectric substrate.[14] With advancements in contact, interface, and defect engineering,[15] the experimental mobility of ml-MoS_2 has improved and typically falls in the range of 50–110 $cm^2 \cdot V^{-1} \cdot s^{-1}$.[9,11,16–18] However, this mobility performance remains a significant bottleneck, as it is still far from the targets required for future 2D transistor applications. For example, Liu *et al.* proposed intermediate- to long-term targets of 200–1000 $cm^2 \cdot V^{-1} \cdot s^{-1}$.[4] To address this challenge, research has focused on modulating both extrinsic and intrinsic scattering mechanisms. On the extrinsic front, strategies such as using HfO_2 substrates to suppress Coulomb scattering have achieved monolayer mobility up to $\sim$150 $cm^2 \cdot V^{-1} \cdot s^{-1}$.[19] Increasing the number of layers is another effective method for mitigating extrinsic scattering.[20,21] Multilayer structures provide enhanced dielectric screening and alleviate the non-uniform vertical distribution of channel carriers,[14,20,21] which moves the transport path further from interface scatterers. This leads to higher mobility than in monolayers, as experimentally demonstrated by the improvement in mean mobility in wafer-scale CVD MoS_2 from $\sim$78 $cm^2 \cdot V^{-1} \cdot s^{-1}$ for monolayer[9] to $\sim$107 $cm^2 \cdot V^{-1} \cdot s^{-1}$ for bilayer.[10] However, to fully leverage the thin-channel advantages of 2D semiconductors, a limited number of layers (ideally, <3 nm) should be emphasized.[4] On the intrinsic front, intervalley scattering between the conduction band minimum (K-valley) and secondary valleys (Q-valleys)

*Corresponding author. Email: xieyu@jlu.edu.cn
© 2026 Chinese Physical Society and IOP Publishing Ltd. All rights, including for text and data mining, AI training, and similar technologies, are reserved.

is known to be the primary channel limiting the intrinsic electron mobility.[22] Strain engineering is a key strategy for manipulating electron and phonon behavior to optimize transport properties.[23,24] For instance, a modest 0.87% tensile strain was shown to increase the mobility of ml-MoS_2 from 50.5 to 127.1 $cm^2 \cdot V^{-1} \cdot s^{-1}$.[25] The twist angle in multilayer structures has also emerged as a new degree of freedom, and previous studies have shown that varying the twist angle can modulate the electronic band structure, thereby affecting carrier mobility.[26,27] However, in contrast to the extensive theoretical studies focused on ml-MoS_2, the intrinsic phonon-limited mobility of multilayer MoS_2 has received insufficient theoretical attention. Focusing on bilayer (bl) systems as one of the most promising thin channels, the ultimate limit of phonon-limited mobility enhancement achieved by suppressing K–Q intervalley scattering via modulation strategies remains unknown.

In this study, we address these questions using systematic first-principles calculations. Our results show that the interlayer interaction in simple 3R (0°) and 2H (60°) stacked bl-MoS_2 does not improve intrinsic transport. Instead, it reduces the room-temperature (300 K) intrinsic mobility to 45 and 35 $cm^2 \cdot V^{-1} \cdot s^{-1}$, respectively, which are far below the calculated monolayer value of 160 $cm^2 \cdot V^{-1} \cdot s^{-1}$. We then propose a "valley separation engineering" strategy that combines twist angle and applied stress to modulate the key electron band features, successfully enhancing this fundamental performance metric. Importantly, we observe a saturation phenomenon in the mobility enhancement, revealing an ultimate phonon-limited mobility limit of ~200 $cm^2 \cdot V^{-1} \cdot s^{-1}$ in modulated bl-MoS_2.

Based on Density Functional Theory (DFT) calculations, the phonon-limited electron mobility (μ_e) was obtained using the linearized iterative Boltzmann transport equation (IBTE) method, as implemented in the Electron-Phonon Wannier (EPW) code[28,29] [see Supplementary Materials (SM) for details]. For comparison, benchmark calculations using the ARES package[30,31] based on the acoustic deformation potential (ADP) approximation, are presented in Fig. 1(a) (dashed lines). The ADP method fails to capture the correct physics. By contrast, the rigorous IBTE results (solid lines) show the trend $\mu_e(\text{ml}) > \mu_e(\text{bl-3R}) > \mu_e(\text{bl-2H})$ as mentioned above. The origin of this severe mobility degradation can be traced to distinct modifications of the electronic band structure induced by interlayer interactions [Figs. 1(b) and 1(c)]. In ml-MoS_2, the conduction-band minimum (CBM) is at the K-point, with a secondary valley at the Q-point, which is approximately 170 meV higher in energy (ΔE_{QK}). However, in bilayer systems, this energy separation is drastically reduced by interlayer interactions, decreasing to 35 meV in bl-3R and −30 meV in bl-2H MoS_2.

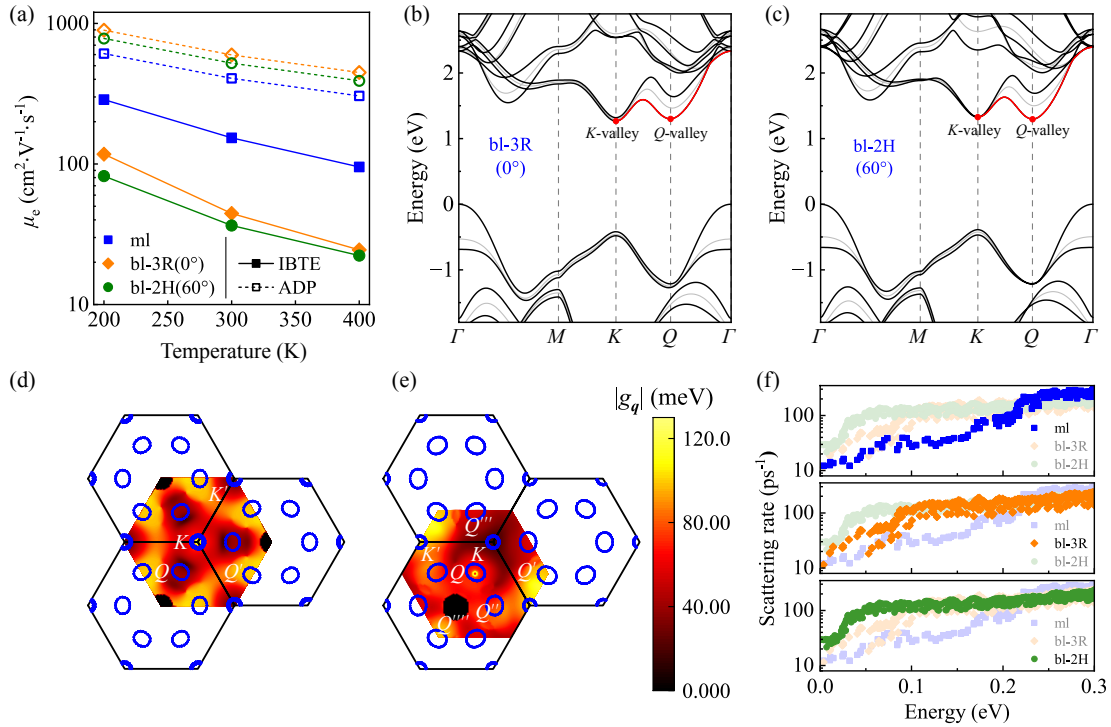

Fig. 1. Mobility degradation in bl-MoS_2 and its intervalley scattering bottleneck. (a) Calculated electron mobility (μ_e) in ml, bl-2H, and bl-3R MoS_2 at temperatures of 200, 300, and 400 K. The vertical axis is plotted on a logarithmic scale. Solid lines represent results calculated using the IBTE method, while dashed lines correspond to results obtained using the ADP approximation. (b) and (c) Calculated band structures of bl-3R (0°) and bl-2H (60°) MoS_2, respectively, compared with ml-MoS_2 (gray solid lines). Red lines highlight the K- and Q-valleys. (d) and (e) Electron-phonon coupling strength distribution $|g_{\boldsymbol{q}}|$ for the CBM electron state at the K-valley (bl-3R) and Q-valley (bl-2H), respectively. The heat map displays phonon wavevector $\boldsymbol{q}$ resolved electron-phonon coupling matrix elements. The black hexagon outlines the electron Brillouin zone, and the blue circles indicate the constant energy surfaces near the CBM. (f) Electron scattering rate as a function of energy (relative to CBM) in ml, bl-2H, and bl-3R MoS_2 at 300 K (the three panels in (f) show the same dataset, with different data series highlighted in each for clarity).

Since earlier theoretical work identified K–Q intervalley scattering as a key mobility-limiting factor in ml-MoS_2,[22] the drastic decrease in ΔE_{QK} in bilayer systems is expected to amplify this scattering channel. To trace this effect, we calculated the electron-phonon coupling (EPC) matrix element $|g_{\boldsymbol{q}}|$ for the CBM states of the two bilayer structures and the energy-dependent scattering rate τ^{-1}. As shown in the EPC strength maps [Figs. 1(d) and 1(e)], the hotspots are located precisely at the phonon wavevectors required to facilitate intervalley scattering, such as the K–Q and Q–Q channels. This provides evidence that intervalley scattering in bl-MoS_2 is mediated by strongly coupled phonons. The activation of this channel is clearly visualized by the scattering rate (τ^{-1}) [Fig. 1(f)]. At a specific energy threshold, a noticeable increase in the density of scattering rate points occurs, signifying the opening of the intervalley channel, and is accompanied by a sharp increase in the scattering rates to over 100 ps^{-1}. For bl-2H MoS_2, this high-density scattering appears almost immediately after the CBM. In bl-3R MoS_2, it emerges at approximately 50 meV, whereas for ml-MoS_2, its appearance is delayed until ∼170 meV. This confirms that, in bilayer systems, the activation of this strong intervalley scattering channel, occurring precisely in the low-energy region near the CBM, has become the dominant bottleneck for phonon-limited electron transport. This finding directly motivates exploration of strategies to separate the conduction-band valleys in bl-MoS_2, thereby suppressing detrimental scattering.

We first explored the twist angle θ as a strategy for modulating the valley structure by constructing a series of twisted bilayer (tb) commensurate supercells (see the SM for supercell construction details), denoted as tb-$MoS_2(\theta)$. Commensurate supercells contain numerous atoms and exhibit complex electronic band structures. For example, figures 2(a) and 2(b) show the atomic structure and corresponding complex band structure for $\theta = 27.8°$, respectively. Although complex band folding makes the original Q-valley difficult to identify, the K-valley states are well preserved and clearly distinguishable as the CBM across various calculated twist angles [Fig. S2 in the SM]. We therefore define the "valley separation" ΔE_{VS} as the energy difference between the lowest conduction-band local minimum (valley) outside the K-valley and the K-valley CBM itself, i.e., $\Delta E_{VS} = E_{\text{non-}K\text{-valley}} - E_K$, which becomes negative when the CBM shifts away from the K-valley. Based on this definition, systematic calculations [Fig. 2(c) and Fig. S2 in the SM] confirm the non-monotonic, volcano-shaped trend for ΔE_{VS} as a function of θ, which is consistent with previous studies, peaking at ∼100 meV near $\theta \approx 30°$. This "volcano" trend is notably inconsistent with the calculated interlayer binding energy E_b (red line, right axis), which remains largely flat from 10° to 50°. This inconsistency suggests that the modulation of ΔE_{VS} is not governed by simple variations in interlayer binding strength.

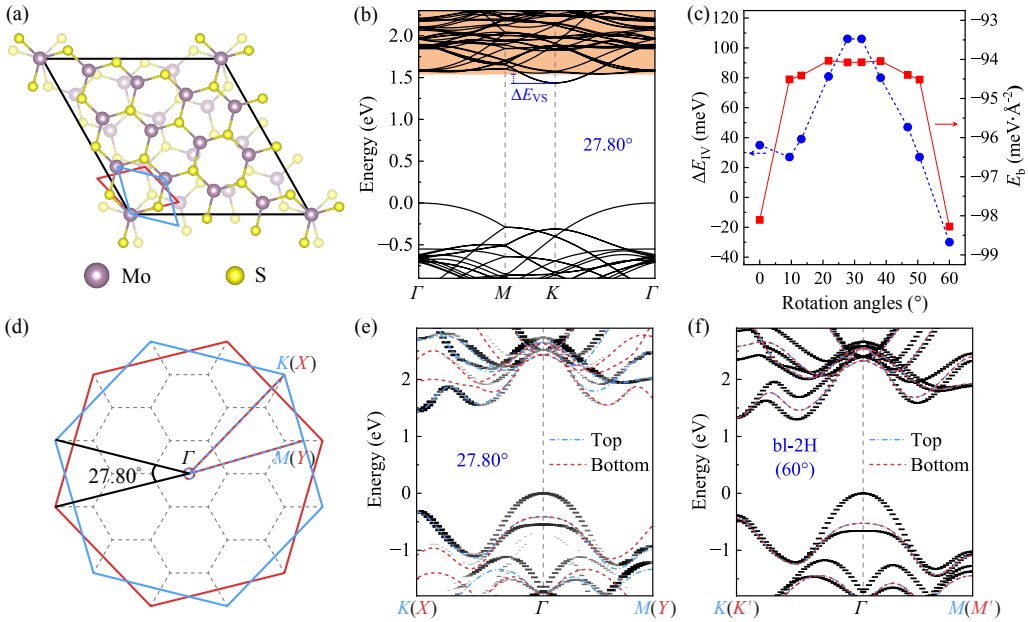

Fig. 2. Electronic structure modulation in bl-MoS_2 by twist angle. (a) Atomic structure of tb-MoS_2(27.80°). The black outline indicates the commensurate supercell. The blue and red outlines indicate the primitive cells of the top and bottom layers, respectively. (b) Calculated band structure of tb-MoS_2(27.80°). The orange shaded area highlights all conduction bands above the secondary valley to emphasize the energy separation. (c) Valley separation (ΔE_{VS}, blue circles with a dashed guideline, left axis) and interlayer binding energy (E_b, red squares with a solid guideline, right axis) as a function of the twist angle θ. (d) Primitive Brillouin zones for the top (blue) and bottom (red) layers in tb-MoS_2(27.80°), illustrating their relative orientation in reciprocal space. The central dashed hexagon is the mini-Brillouin zone of the supercell. High-symmetry points of the top layer (K, Γ, M) and their corresponding projections on the bottom layer (X, Γ, Y) are labeled. (e) Unfolded effective band structure (EBS) of tb-MoS_2(27.80°). The color intensity of the black points represents the projection weight onto the top layer's primitive high-symmetry path (K–Γ–M). The blue dash-dot and red dashed lines are the pristine band structures of the top and bottom monolayers, plotted along the K–Γ–M and X–Γ–Y paths, respectively. (f) Unfolded EBS of bl-2H (60°) MoS_2, with all plot notations consistent with (e).

To more clearly analyze the complex supercell band structures (which arise from band folding), we employed the band unfolding technique to calculate the effective band structure (EBS),[32] a well-established tool for analyzing twisted bilayer systems.[26] Close inspection of the unfolded EBS for tb-MoS_2(27.80°) [Fig. 2(e)] reveals that the lowest conduction band almost perfectly follows the lower envelope of the pristine monolayer conduction bands (blue and red lines), with significant deviation only in a small region around the Γ-point. In sharp contrast, the EBS of bl-2H (60°) MoS_2 shows that its conduction band exhibits strong reconstruction, deviating significantly from the monolayer envelopes across the entire Brillouin zone. This difference stems from the wavevector mismatch for $\boldsymbol{k}$-states away from Γ (i.e., $\boldsymbol{k} \neq 0$) caused by the twist angle, which reduces the effect of the interlayer interaction on the conduction band features. The suppression of band reconstruction is evident in the systematic evolution from 0° to 30° (Fig. S3 in the SM) and is maximized near $\theta \approx 30°$. Consequently, the monolayer conduction-band features are preserved over a large portion of the Brillouin zone, yielding the largest ΔE_{VS}. Although the twist angle is an effective modulation strategy, the maximum achievable E_{VS} (≈100 meV) is still significantly lower than that of ml-MoS_2 (≈170 meV), which is insufficient to fully suppress intervalley scattering.

We introduced applied stress as part of a combined strategy to further enhance the valley separation ΔE_{VS} in bl-MoS_2. We systematically studied four distinct stress conditions: in-plane (*ab*-plane) biaxial tension (BT-*ab*), in-plane biaxial compression (BC-*ab*), *c*-axis uniaxial compression (UC-*c*), and hydrostatic compression (HC). Considering tb-MoS_2(27.80°) under UC-*c* stress as an example [Fig. 3(a)], as the stress increases (indicated by darker colors), the energy of the secondary valley increases, thereby enhancing ΔE_{VS}. A quantitative comparison of the four stress conditions shown in Fig. 3(b) reveals that BT-*ab* and UC-*c* effectively enhance the valley separation in both tb-MoS_2(27.80°) (solid lines) and bl-2H MoS_2 (dotted lines). Driving ΔE_{VS} to large negative values (e.g., BC-*ab* and HC) also achieves valley separation by isolating the non-*K* valleys. However, considering the *K*-valley's lighter effective mass and lower degeneracy, we focused on preserving the *K*-valley CBM (positive ΔE_{VS}) to realize high-mobility transport (see Fig. S4 in the SM for a representative comparison). Notably, Fig. 3(b) also demonstrates that the ΔE_{VS} responses to stress for these two structures are parallel. Moreover, the band feature responses for all five representative twist angles (0°, 13.17°, 21.79°, 27.80°, and 60°) under the four stress conditions (Fig. S5 in the SM) confirm that this stress modulation behavior is nearly identical across structures with different twist angles.

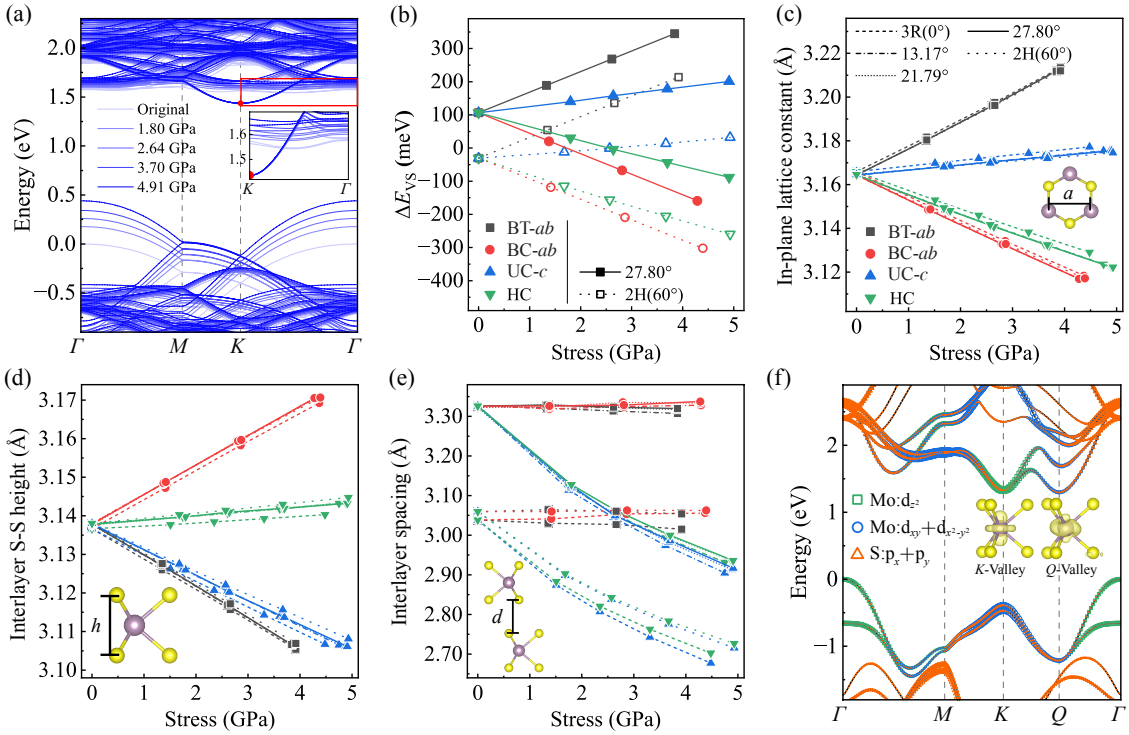

Fig. 3. Electronic structure modulation in bl-MoS_2 by applied stress and its underlying mechanisms. (a) Evolution of the band structure for tb-MoS_2(27.80°) under increasing UC-*c* stress (darker colors correspond to higher stress). The bands are aligned to the CBM at the *K*-point (marked by the red dot) for comparison. The inset provides a magnified view of the CBM region, highlighting the upward energy shift of the secondary valley with increasing stress. (b) The valley separation, ΔE_{VS}, as a function of applied stress for tb-MoS_2(27.80°) (solid lines, filled markers) and bl-2H MoS_2 (dotted lines, hollow markers) under the four stress conditions (BT-*ab*, BC-*ab*, UC-*c*, and HC). (c) In-plane lattice constant *a*, (d) intralayer S-S height *h*, and (e) interlayer spacing *d* as a function of applied stress. Data for all five representative twist angles (0°, 13.17°, 21.79°, 27.80°, and 60°) are plotted, with the legend in (c) applying to (c)–(e). The tightly clustered trend lines for each stress type show a highly uniform response across all twist angles. Insets show schematics of the corresponding structural parameters. (f) Orbital-resolved band structure of bl-2H MoS_2. The insets show the corresponding partial charge densities for the *K*-valley and *Q*-valley states.

Given the consistent stress response mentioned above, we analyzed the physical origin of this modulation, starting with the orbital components of bl-2H MoS_2. As shown in Fig. 3(f), the K and Q valleys have differing orbital characteristics: the K valley is primarily composed of out-of-plane Mo:d_{z^2} orbitals, whereas the Q valley is dominated by in-plane Mo:$d_{xy}/d_{x^2-y^2}$ and S:p_x/p_y orbitals. This distinction is visually reflected in the partial charge densities of the two valley states, as shown in Fig. 3(f) inset, and for twisted structures such as tb-MoS_2(27.80°), similar partial charge density features for the CBM and secondary valley are also preserved (Fig. S6 in the SM). This difference in spatial distribution implies that ΔE_{VS} is sensitive to two deformation pathways: (i) "flattening" the MoS_2 unit (reducing intralayer height h), which intensifies the in-plane Coulomb repulsion and thus primarily raises E_Q (dominated by in-plane orbitals); and (ii) "widening" it (increasing in-plane lattice a), which lessens the Coulomb confinement on the out-of-plane d_{z^2} orbital and thus primarily lowers E_K. Key structural data presented in Figs. 3(c)–3(e), which plots the responses of the in-plane lattice a, intralayer height h, and interlayer spacing d (schematics in the insets), verify this mechanism and explain the efficiency differences observed in Fig. 3(b). For BT-*ab* (black squares), its primary "widening" effect [$a\uparrow \rightarrow E_K\downarrow$, Fig. 3(c)] is accompanied by a Poisson-effect-induced "flattening" [$h\downarrow \rightarrow E_Q\uparrow$, Fig. 3(d)]. These two beneficial distortions synergize, leading to the highest efficiency in enhancing ΔE_{VS}. In contrast, UC-*c* (blue triangles) also activates both "flattening" and "widening" effects, but its efficiency is far lower. This is attributed to the dual buffering effect: (1) Structural Buffering: Comparison of Figs. 3(e) and 3(d) (blue triangles) shows that the *c*-axis pressure is overwhelmingly absorbed by the soft interlayer vdW gap (d decreases sharply), leaving the intralayer geometry almost unaffected, resulting in a very weak "flattening" (a minimal decrease in h). (2) Electronic Competition: The compression of d enhances the interlayer interaction, which, as discussed earlier, is a detrimental factor that counteracts ΔE_{VS} enhancement. Conversely, the BC-*ab* and HC stress conditions fail to induce "flattening" and "widening" of the MoS_2 unit, thus leading to a decrease in ΔE_{VS}.

Based on the above analysis, we employed a "valley separation engineering" strategy by combining a twist angle near 30° with in-plane biaxial tension (BT-*ab*) and out-of-plane uniaxial compression (UC-*c*). Through this strategy, the valley separation ΔE_{VS} in bl-MoS_2 is enhanced to ∼350 meV, exceeding the intrinsic value of ml-MoS_2 (∼170 meV), and is expected to increase further with increasing stress. This modulation of the electronic structure is reflected in the phonon-limited electron mobility (μ_e) calculated at 300 K, as shown in Fig. 4(a). Starting with the stress-free data points (diamonds), we observed that tb-MoS_2(27.80°) exhibits a mobility of 85 $cm^2\cdot V^{-1}\cdot s^{-1}$, which is more than double that of bl-2H (35 $cm^2\cdot V^{-1}\cdot s^{-1}$). Subsequently, the application of stress leads to a further increase in mobility. Notably, as ΔE_{VS} continues to increase, the mobility of these bilayer structures is ultimately

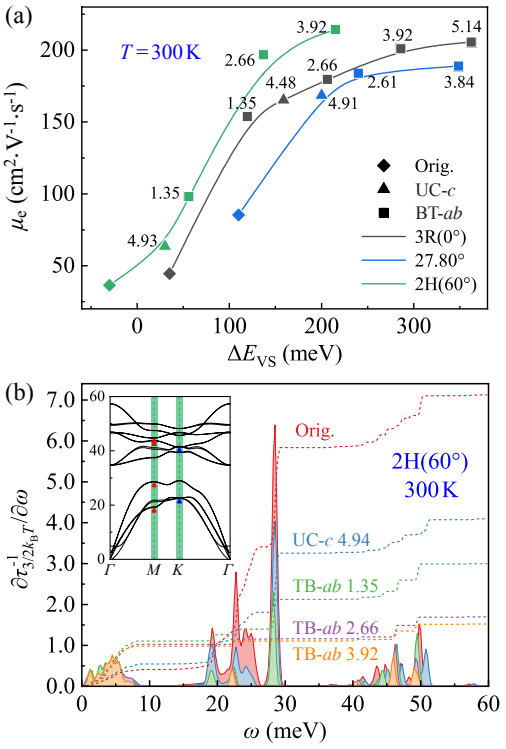

Fig. 4. Electron mobility of bl-MoS_2 under combined modulation. (a) Calculated electron mobility (μ_e) at T = 300 K as a function of valley separation (ΔE_{VS}). The data points distinguish the stress conditions: original (Orig., diamonds), uniaxial compression (UC-*c*, triangles), and biaxial tension (BT-*ab*, squares). Colors represent the structures: bl-3R (0°) (gray), tb-MoS_2(27.80°) (blue), and bl-2H (60°) (green). The connecting lines are guides for the eye, and the numbers indicate the magnitude of applied stress in GPa. (b) Spectral decomposition of the scattering rate for a representative electron at an energy of $3/2\,k_BT$ as a function of phonon energy (ω) at 300 K for bl-2H MoS_2 under different stresses. Solid curves denote the differential scattering rate ($\partial\tau^{-1}/\partial\omega$), and dashed lines show the corresponding cumulative integral, illustrating the relative contribution of different phonon energy ranges to the total scattering rate. The labels on the dashed curves indicate the stress type and its magnitude in GPa. The inset shows the phonon dispersion of pristine bl-2H MoS_2, where green shaded regions highlight the M-point and K-point phonons responsible for intervalley scattering, with the triangles marking the specific dominant phonon modes.

enhanced to ∼200 $cm^2\cdot V^{-1}\cdot s^{-1}$, exhibiting a clear saturation behavior of the modulation.

We analyzed the spectral decomposition of the electron-scattering rate [Fig. 4(b)] using the method developed by Poncé *et al.*,[33] taking bl-2H MoS_2 as an example. Based on the mobility trend shown in Fig. 4(a), we identified two regimes. As the valley separation initially increases, the rapid increase in mobility is primarily attributed to the suppression of intervalley scattering channels. Referring to the phonon dispersion in the inset, the scattering peak corresponding to the M-point phonon at a phonon energy of ∼28.5 meV is dramatically suppressed by stress (e.g., the peaks vanish in the purple and orange curves), which is also reflected in the cumulative scattering rate (dashed lines), where the sharp

step in this energy range disappears. Similarly, scattering from the K-point phonon (e.g., ∼22.7 meV) is also significantly reduced. However, a residual contribution remains even under the largest applied stresses, likely originating from scattering between the degenerate CBM valleys. These results validate the effective suppression of intervalley scattering. Once intervalley scattering is effectively suppressed, the mobility tends to saturate. Previous studies have shown that tensile stress can further reduce the electron effective mass at the CBM of bl-2H MoS_2,[34] which is expected to continuously improve mobility; however, our spectral analysis reveals a critical counteracting mechanism. As shown in Fig. 4(b), under increased stress (e.g., >1.35 GPa), the cumulative scattering rate in the low-energy region surpasses that of the stress-free structure. This indicates that stress-induced phonon softening, also manifested as a downshift of the scattering rate spectral peaks under stress, significantly intensifies the intravalley scattering dominated by low-energy acoustic phonons. This behavior differs from that of ml-MoS_2, where the reduction in scattering rates dominates, leading to a continuous increase in mobility under 0%–5% tensile strain.[35] In a bilayer system, the enhanced intravalley scattering caused by phonon softening offsets the benefits of the reduced effective mass. Consequently, an upper limit emerges in the intrinsic mobility modulation after intervalley scattering is suppressed.

It is worth noting that our calculated intrinsic mobilities for pristine bl-2H and bl-3R MoS_2 are lower than the reported experimental values. This is mainly because GGA functionals underestimate the K–Q valley separation (ΔE_{QK}) in MoS_2, with the experimental value for bl-2H being (89 ± 9) meV[36] (compared to −30 meV calculated), which leads to an overestimation of intervalley scattering. Nevertheless, our results correctly reproduce the experimental trend[36] of a dramatic reduction in ΔE_{QK} from monolayer to bilayer, thereby capturing the scattering physics unique to bilayer systems. In addition, experimental observations exhibit significant complexity. On the one hand, the layer dependence of mobility is not monotonic. While thicker layers often exhibit higher mobility owing to reduced extrinsic scattering,[20,21] it has also been observed in clean environments, such as in devices utilizing van der Waals heterostructure platforms[37] or via *in situ* vacuum annealing to remove atmospheric contamination,[38] that the mobility of ml-MoS_2 can be superior to that of its bilayer or trilayer counterparts, a trend consistent with our theoretical prediction. On the other hand, experimental reports regarding the mobility difference between bl-2H and bl-3R are inconsistent; while some studies report that the 3R phase significantly outperforms the 2H phase,[39,40] others suggest a less drastic contrast.[10] These phenomena collectively suggest that the roles of substrates and dielectrics extend beyond dielectric screening and remote phonon scattering. These components are likely to alter the fine electronic structure through strain or proximity effects, thereby significantly influencing the scattering channels.

Therefore, to fully resolve these issues, it is crucial for future theoretical studies to combine high-precision computational methods (such as hybrid functionals to improve band accuracy) with atomic-scale modeling of realistic environments (to account for environmental interactions). However, owing to the difficulty in adapting nonlocal Fock exchange terms to the traditional DFPT framework and the prohibitively high computational costs, their application remains limited. The recent progress in machine learning Hamiltonians[41,42] offers a promising path forward. Despite these challenges, our "valley separation engineering" strategy increases ΔE_{VS} to a range far exceeding the thermal excitation at room temperature, effectively bypassing the impact of the initial underestimation of ΔE_{VS}. Consequently, the value of $\sim 200\,\mathrm{cm^2 \cdot V^{-1} \cdot s^{-1}}$ obtained in the saturation regime reflects the intrinsic transport upper limit after the intervalley scattering bottleneck is removed, thereby providing a reasonable physical reference for understanding and optimizing the ultimate performance of bilayer MoS_2.

Acknowledgements. This study was supported by the National Key R&D Program of China (Grant No. 2022YFA1402503), and the High Performance Computing Center of Jilin University, China.

References

[1] Moore G E 1965 *Electronics.* **38** 114
[2] Yan R H, Ourmazd A, and Lee K F 1992 *IEEE Trans. Electron Devices* **39** 1704
[3] Uchida K, Koga J, and Takagi S I 2007 *J. Appl. Phys.* **102** 074510
[4] Liu Y, Duan X D, Shin H J *et al.* 2021 *Nature* **591** 43
[5] *IEEE International Roadmap for Devices and Systems (IRDS) Beyond CMOS and Emerging Materials Integration* (Institute of Electrical and Electronics Engineers, 2023) [Online]. Available: https://doi.org/10.60627/0p45-zj55 [Accessed: 10th Nov. 2025]
[6] Wang S, Liu X, and Zhou P 2022 *Adv. Mater.* **34** 2106886
[7] Jiang X, Wang Z K, Li C *et al.* 2024 *Chin. Phys. Lett.* **41** 057501
[8] Li M S, Li H M, and Liu S 2024 *Chin. Phys. Lett.* **41** 027501
[9] Li T, Guo W, Ma L *et al.* 2021 *Nat. Nanotechnol.* **16** 1201
[10] Liu L, Ma L, Li W S *et al.* 2022 *Nature* **605** 69
[11] Zou X, Zhao Y Y, Fan D X *et al.* 2025 *Science* **390** aea0849
[12] Kaasbjerg K, Thygesen K S, and Jacobsen K W 2012 *Phys. Rev. B* **85** 115317
[13] Poncé S, Royo M, Stengel M *et al.* 2023 *Phys. Rev. B* **107** 155424
[14] Yu Z, Ong Z Y, Li S L *et al.* 2017 *Adv. Funct. Mater.* **27** 1604093
[15] Wei C, Jiazila N, Liu X Y *et al.* 2024 *Chin. Phys. Lett.* **41** 128501
[16] Radisavljevic B and Kis A 2013 *Nat. Mater.* **12** 815
[17] Liu Y, Wu H, Cheng H C *et al.* 2015 *Nano Lett.* **15** 3030
[18] Shen P C, Su C, Lin Y X *et al.* 2021 *Nature* **593** 211
[19] Yu Z H, Ong Z Y, Pan Y M *et al.* 2016 *Adv. Mater.* **28** 547
[20] Li S L, Wakabayashi K, Xu Y *et al.* 2013 *Nano Lett.* **13** 3546
[21] Liang B X, Liu L H, Tang J C *et al.* 2023 *Chin. Phys. Lett.* **40** 058503
[22] Li X D, Mullen J T, Jin Z H *et al.* 2013 *Phys. Rev. B* **87** 115418
[23] Ge Y F, Wan W H, Feng W X *et al.* 2014 *Phys. Rev. B* **90** 035414

[24] Sun J, Meng H, Guo R L *et al.* 2025 *Chin. Phys. Lett.* **42** 110701
[25] Chen Y, Lu D L, Kong L G *et al.* 2023 *ACS Nano* **17** 14954
[26] Tan Y, Chen F W, and Ghosh A W 2016 *Appl. Phys. Lett.* **109** 101601
[27] Liao M Z, Wei Z, Du L J *et al.* 2020 *Nat. Commun.* **11** 2153
[28] Lee H, Poncé S, Bushick K *et al.* 2023 *npj Comput. Mater.* **9** 156
[29] Poncé S, Margine E R, and Giustino F 2018 *Phys. Rev. B* **97** 121201
[30] Xu Q, Wang S, Xue L T *et al.* 2019 *J. Phys.: Condens. Matter* **31** 455901
[31] Xue L T, Xu Q, Ma C *et al.* 2024 *Phys. Rev. B* **110** 155157
[32] Popescu V and Zunger A 2012 *Phys. Rev. B* **85** 085201
[33] Poncé S, Schlipf M, and Giustino F 2019 *ACS Energy Lett.* **4** 456
[34] Dong L, Dongare A M, Namburu R R *et al.* 2014 *Appl. Phys. Lett.* **104** 053107
[35] Du G, Li C, and Cheng L 2023 *Phys. Rev. B* **107** 085422
[36] Dou X 2014 *ACS Nano* **8** 7458
[37] Cui X 2015 *Nat. Nanotechnol.* **10** 534
[38] Lembke D, Allain A, and Kis A 2015 *Nanoscale* **7** 6255
[39] Zhang X M, Nan H Y, Xiao S Q *et al.* 2019 *Nat. Commun.* **10** 598
[40] Li X, Shi X H, Marian D *et al.* 2023 *Sci. Adv.* **9** eade5706
[41] Li H, Tang Z C, Fu J H *et al.* 2024 *Phys. Rev. Lett.* **132** 096401
[42] Zhong Y, Liu S X, Zhang B H *et al.* 2024 *Nat. Comput. Sci.* **4** 615